








Omnipresent authigenic calcite distorts Arctic radiocarbon chronology

Jutta Erika Wollenburg ¹✉, Jens Matthiessen ¹, Christoph Vogt ², Gernot Nehrke ¹, Hendrik Grotheer ¹, Dorothee Wilhelms-Dick¹, Walter Geibert ¹ & Gesine Mollenhauer ^{1,2}

As calcareous foraminifera precipitate their shells from the surrounding water mass, they are the basis of most marine radiocarbon chronologies and paleo-proxies. Nevertheless, post-mortem alteration of shells, especially addition of authigenic calcite, impact proxy records. In the Arctic Ocean, authigenic calcite overgrowth on foraminifera has been attributed to hydrocarbon release, with a single report on ¹³C-enriched authigenic calcite, indicating a different carbon source. Here, we use comparative radiocarbon, carbon and oxygen isotope measurements to show that this ¹³C-enriched authigenic calcite impacts a large proportion of Holocene and the majority of last glacial planktonic foraminifera in the Arctic Basin. This authigenic precipitated calcite is ¹⁴C-depleted, so overgrowth results in invariably older ¹⁴C-ages. We show that, in comparison with published data, the true chronology of Arctic basin sediments can deviate by more than 10,000 years in critical parts of the last deglaciation and that stable oxygen and carbon isotopes, as likely all calcite-based proxy-records are affected with potential implications for paleoclimate models.

¹ Alfred Wegener Institute, Helmholtz Centre for Polar and Marine Research, Bremerhaven, Germany. ² Geosciences and MARUM, University of Bremen, Bremen, Germany. ✉email: jutta.wollenburg@awi.de

As the Arctic Ocean warms twice as fast as the lower latitude oceans¹, the timing and extent of past climate changes recorded in Arctic sediments is of utmost importance to ground-truth climate model projections^{2,3} of future Arctic and world-ocean climate scenarios. Radiocarbon (¹⁴C) dating on calcareous foraminifera^{4–9} provides the most trustworthy and stringent chronology for such ground-truthing in the last 45 ka.

Radiocarbon forms in the stratosphere, enters the ocean in oxidized form and finally becomes incorporated in shells, where radioactive decay results in decreasing ¹⁴C levels over time, ideally recording the date of death of the animal¹⁰. However, calcareous shells are prone to postmortem diagenetic modifications^{10–14}. Shells first and foremost encompass dissolution at the sediment-water interface, and within the uppermost cm of the sediments, these modifications are largely driven by metabolic CO₂ released from the mineralization of organic matter¹⁵.

Diagenetic alteration of foraminifera shells by authigenic calcite overgrowth (hereafter overgrowth) has often been linked to situations where CO₂ is provided by either the microbial oxidation of methane or the microbial anaerobic degradation of labile organic matter^{11,16}. Precipitation then involves a subsequent increase in pH and carbonate saturation state to pH >8.0 and Ω >5 by the anaerobic oxidation of methane or sulfate or iron reduction^{17,18}. Therefore, observations of authigenic carbonate precipitation in the world's oceans are essentially limited to regions with methane emanation or high labile organic carbon accumulation^{18–21}. Notably, carbonate precipitates resulting from both the oxidation of methane and organic matter are expected to feature depleted δ¹³C and ¹⁴C signatures, the latter resulting in an age bias to older ages^{11,22,23}.

Overgrowth also alters oxygen, boron isotope^{19,24–26} and trace metal/Ca^{16,25} ratios by incorporation of respective exogenous elements. This is extremely critical for the Arctic Ocean because here, >45 ka-chronology, and most assumptions about the extent and direction of paleoenvironmental change essentially rely on these paleoceanographic proxies^{8,27,28}.

Here, we provide the first comprehensive documentation on the late Pleistocene to Holocene preservation state of the dominant (>90%) calcareous planktonic foraminifera *Neogloboquadrina pachyderma*, used both for establishing a chronology and palaeoceanographic change in the Arctic Ocean^{5,27,28}.

We use paired stacked stereo (hereafter stereo) and scanning electron microscopy (SEM) images to illustrate progressive overgrowth with depth. Using a mini carbon dating system (MICADAS)^{29,30} it is possible to obtain ¹⁴C ages on samples consisting of only 20–60 *N. pachyderma* specimens in contrast to approximately 1 mg C equivalent to a minimum of 1000 specimens required for standard AMS analyses. Such small sample sizes allow to carefully inspect and document all shells prior to ¹⁴C measurement, and to carry out multiple comparative measurements on shells with different degrees of overgrowth. We also include comparative studies on stable carbon and oxygen isotopes in order to exemplify the impairment of paleoceanographic proxies by overgrowth.

This study focuses on the consistently foraminiferal-rich core PS72/413-3 supplemented by analyses on PS2185-6 to investigate the impact of overgrowth on the chronology of a core previously used for Arctic-wide correlations⁴ (Fig. 1 and Supplementary Tables 1 and 2). Qualitative inspections on surface sediments document the widespread phenomenon.

Results

Morphological description of overgrowth and authigenic precipitates. *Neogloboquadrina pachyderma* precipitates a porous,

translucent, multichambered, Mg-poor calcite shell³¹. The primary shell is multilamellar, and with each new chamber added, an additional layer is deposited on the older chambers^{32,33}. On the outside conical protuberances protrude above the smooth porous microcrystalline shell, the inner surface of the wall is smooth (Fig. 2a–c)^{34,35}. Primary shells are prone to dissolution and therefore are rare in Arctic Ocean sediments^{36–39}. Here, most specimens have precipitated an outer secondary calcite crust on the primary shell (Fig. 2d–g)^{32,35,40,41}. Two principal types of secondary calcite crust are observed on the shell surface. The reticulate type is characterized by polygonal ridges that surround a variable large smooth area around the pore pits⁴² (Fig. 2e, g). In the crystalline type, large euhedral crystals with growth facets on the crystal faces form around the pores⁴² (Fig. 2e, f). The reticulate and crystalline form, and intergrades between these two, are often found on the same shell.

Whether primary or secondary shell type, any unaltered biogenically precipitated *N. pachyderma* shell is translucent, and AMS, isotope and trace metal data should only be obtained from such shells^{12,13,25}. However, such ideal shells are rare in Arctic sediment cores where samples are usually dominated by white¹² or even brownish discolored shells (see <https://www.pangaea.de/?q=doi:10.1594/PANGAEA.938246>, plate 2 in Eynaud et al.³⁸). Hereby, not only in shells with overgrowth but also in those affected by dissolution the radiocarbon age, and the carbon and oxygen isotope value should differ^{10,12–14,25,43–45}.

Consequently, in this paper, only a translucent *N. pachyderma* shell with surface textures as described is regarded as unaltered by diagenetic processes, as pristine specimen. In contrast, an increasingly whitish discoloration of the shell reflects increasing diagenetic change (dissolution or initial overgrowth) (Fig. 2i), and a color alteration to the light yellow-brown spectrum indicates major overgrowth (Fig. 3a, b)⁴⁶.

Initial overgrowth is characterized by minute discrete authigenic crystallites (<0.5–1 μm) precipitated at various places on the shell, best seen on the otherwise perfectly smooth shell of the benthic foraminifera *Cassidulina neoteretis* (Fig. 2c, f–h). Thereafter, the number of crystallites increases first laterally to form closed sheets around the shells which do not alter the original shape of the foraminifera, then in thickness (Fig. 2h–m). Overgrowth usually shows a porous appearance, less commonly a sheet of tetrahedral calcite crystals (Fig. 2k–m) or larger (>10 μm) crystals sticking out from the shell.

Aksu and Vilks³⁷ reported authigenic Mg-calcites on foraminiferal shells from surface sediments of the CESAR, LOREX and FRAM sites. In this study, shells from randomly selected surface sediments of the central Arctic Ocean reveal overgrowth and crystals at all sites (Fig. 1).

In contrast to overgrowth, co-occurring authigenic calcite crystals (hereafter crystals) display a large morphological variability from xenomorphic or microcrystalline envelopes surrounding clusters of planktonic foraminiferal shells to microcrystalline spheres, dumbbell-like forms, wheat-sheaf-like bundles, rhombohedra, needle-like forms or even crusts (Fig. 3c–o).

Optical and geochemical characterization of overgrowth.

Energy-dispersive X-ray spectroscopy (EDS) analyses identify the biogenic shell, overgrowth and sedimentary crystals as low Mg-calcite (see <https://www.pangaea.de/?q=doi:10.1594/PANGAEA.938246>). This is in contrast to the findings by Aksu and Vilks³⁷, who reported authigenic high Mg-calcites on large foraminiferal shells from central Arctic surface sediments. But individual measurements were not reported and their maximum value of 10 mol% Mg-calcite (corresponding to about 2.5 weight % Mg)

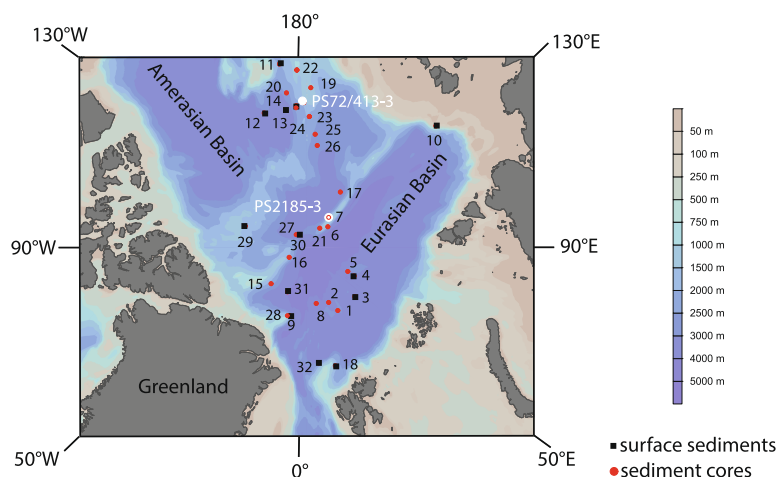


Fig. 1 Map with the investigated core sites (see Supplementary Table 1 for the core locations). Studied sediment cores (white), sediment records whose chronologies are probably affected by overgrowth (red). Surface sediments with overgrowth on foraminifer specimens (black). Bathymetric map created by Ocean Data View version 5.6.2⁹⁸.

corresponds to the minimum value for this mineral. Occasional Mg concentrations >2.5 weight % observed in some of our specimens with porous overgrowth are likely attributed to clay impurities, not to Mg-calcite, due to simultaneously elevated Al and Si contents, and we assume that such a contamination also affected some of the reported specimens of Aksu and Vilks³⁷.

In the Arctic Basin, sediments are derived either from sea-ice, icebergs or collapsing ice-sheets⁴⁷. Whereas sea-ice mainly incorporates fine-grained shallow-water sediments, barren or low in planktonic foraminifer shells⁴⁸, icebergs and ice shelves can erode shelf and upper slope sediments and release incorporated fossil shells during their passage⁴⁹. Consistent with the important role of Arctic shelves on iron supply⁵⁰, an increasing brownish discoloration is observed in, e.g., Pliocene benthic foraminifera fossilized there and transported by glacial iceberg/ice shelves to be released in the Arctic Basin (e.g., Figure 2 of Geibert et al.⁴⁹).

High abundances of such brownish discolored Pliocene benthic species indicate that also the planktonic assemblage and proxies connected to them are unreliable. Consequently, brownish discolored planktonic foraminifera were excluded, as they could either be allochthonous or encrusted by obvious overgrowth²². However, in no analyzed sample, the benthic foraminifera community indicated a strong allochthonous component.

Sediment or authigenic coatings of various kinds may also be deposited on the shell's interior (termed "infillings" here), and were excluded to the best of our knowledge.

In this study, we did comparative measurements on the best-preserved translucent to white and similar-colored foraminifera with and without overgrowth in each sample.

Preservation statuses of measured shells (Fig. 4) are categorized as follows: Pristine, translucent specimen visually free of overgrowth = Preservation Index (PI)₁ category; specimens visually free of overgrowth (PI)₂; and those with overgrowth (PI)₃. PI₁ specimens are generally extremely rare and at depths >5 cm contrast strongly with the predominant foraminifera shell assemblage in both cores. Due to distinctively lower abundances of planktonic foraminifera, PI₁ radiocarbon age could not be studied in core PS2185-6. Our high-resolution measurements,

therefore, focused on the predominant translucent-white to white shells classified as PI₂ and PI₃ regarded as autochthonous shell assemblage. If possible, only translucent-white shells were used for measurements; however, in both cores below 10 cm sediment depth, progressively more white shells had to be picked to meet the weight requirements for the measurements. In all samples, the PI₂ and PI₃ specimens measured matched in terms of shell coloration and we consider them to be deposited at the same time.

The impact of overgrowth on isotope (Fig. 5 and Supplementary Tables 3 and 4) and radiocarbon measurements (Fig. 6 and Supplementary Tables 5 and 6). Carbon isotope analyses in both cores reveal that PI₃ specimens are enriched in ¹³C compared to PI₂ and the majority of crystals have $\delta^{13}\text{C}$ values of >2.5 – 5.6 ‰ (Fig. 5a, b, e, f and Supplementary Tables 3 and 4). Thus, the maximum and mean offset of PI₃ vs PI₂ specimens are 0.75 and 0.31‰ and 0.88 and 0.44‰ for cores PS72/413-3 and PS2185-6, respectively. However, as the mean offset of crystals vs PI₂ species is 3.89 and 3.99‰ for cores PS72/413-3 and PS2185-6, respectively, the $\delta^{13}\text{C}$ value of each PI₃ specimen essentially depends on the extent of overgrowth.

Different to carbon, in core PS72/413-3 the direction of oxygen isotope PI₃ vs PI₂-offset is not constant but maximum values of -1.63 and $+1.03$, respectively, are observed. In core PS2185-6 the PI₃ vs PI₂ -offset is usually positive with maximum and mean values of 1.83 and 0.66‰, respectively.

The extreme $\delta^{18}\text{O}$ differences in small vs large crystals within one sample in core PS72/413-3 with mean offsets of 8.05‰ and extreme low values of up to -13.5 ‰ for large crystals are striking. In core PS2185-6, only large crystals were measured with the lowest values of -0.45 ‰ at 20.5 cm sediment depth. In PS2185-6, only the carbon and oxygen isotopes of PI₃ specimens resemble published values⁴ whereas those of PI₂ specimens deviate. Carbon and oxygen analyses on different crystals in core PS72/413-3 reveal large scatter even within a single sample; thus, the *N. pachyderma* offset due to overgrowth cannot be predicted.

In core PS72/413-3, a few single and replicate radiocarbon measurements on PI₁ specimens from Holocene sediments

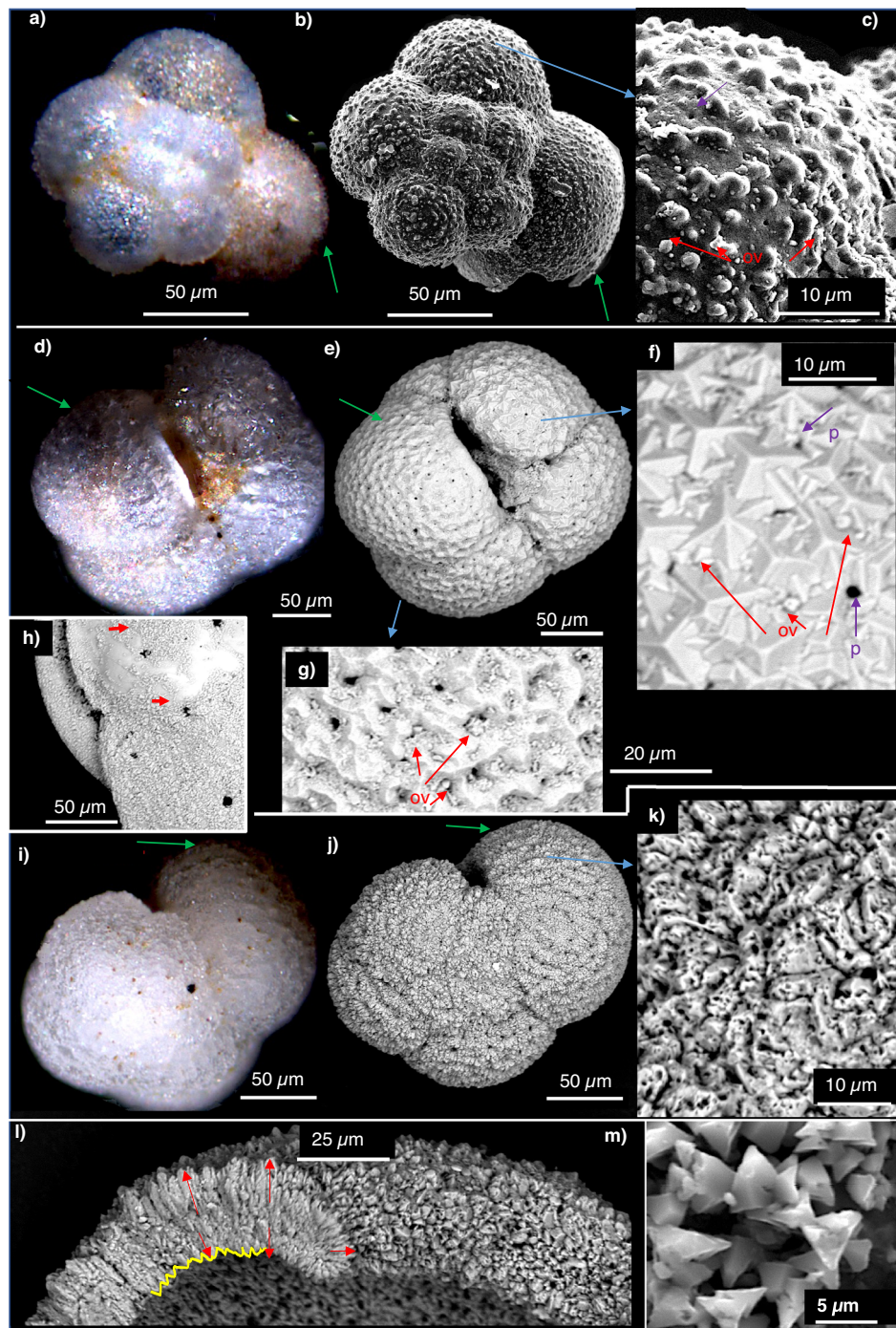


Fig. 2 Axio Zoom and SEM images of overgrowth. **a–c** Translucent *N. pachyderma* with primary shell and little overgrowth in the penultimate chamber and sediment-infilling in the last chamber. **d–g** Translucent *N. pachyderma* specimen with secondary calcite crust and minor $\leq 1\text{--}2\text{-}\mu\text{m}$ -sized authigenic crystallites in depressions on the crystalline (**f**) and reticulate crust (**g**). The overgrowth often clogs the pores and contrasts with the smooth reticulate surface texture and the euhedral biologically precipitated crystals. **h** *Cassidulina neoteretis* (benthic foraminifera) patches of $\leq 1\text{--}2\text{-}\mu\text{m}$ -sized authigenic crystallites on the otherwise smooth shell. **i–k** *N. pachyderma* encrusted by porous overgrowth. **k** At magnifications $>4500\times$ the porous structure of the overgrowth becomes apparent. **l** Cross-section through the last chamber of a different specimen shows tetrahedral overgrowth on the outer and inner shell wall (see the deviation from the usually smooth inner wall), but also authigenic calcite penetrating into the originally porous shell wall⁹⁹. **m** Closed tetrahedral overgrowth. **a, d, i** stacked Axio Zoom, **b–d, g–h, j–m** SEM images. **a–k, m** PS413-3, **l** (PS2185-6). Core depth (cm) **a–c** 3.5, **d–g** 0.5, **h** 3.5, **i–k** 22.5, **l, m** 10.5. Arrows: green = last chamber, blue = penultimate chamber, red = authigenic crystals, purple = pore. Yellow line highlights the rough shell interior.

(Fig. 5b and Supplementary Table 5) reveal radiocarbon ages (hereafter ages) comparable to those of PI₂ specimens. PI₁-plateaus at 15.5–19.5 and 20.5–23.5 cm are attributed to down-core displacement by bioturbation (for discussion see methods).

The ages of PI₂ and PI₃ specimens increase with core depth, hereby, PI₂ shells are invariably younger than PI₃ shells (Fig. 5a, d). The age offset ranges from a few hundred to thousands of years.

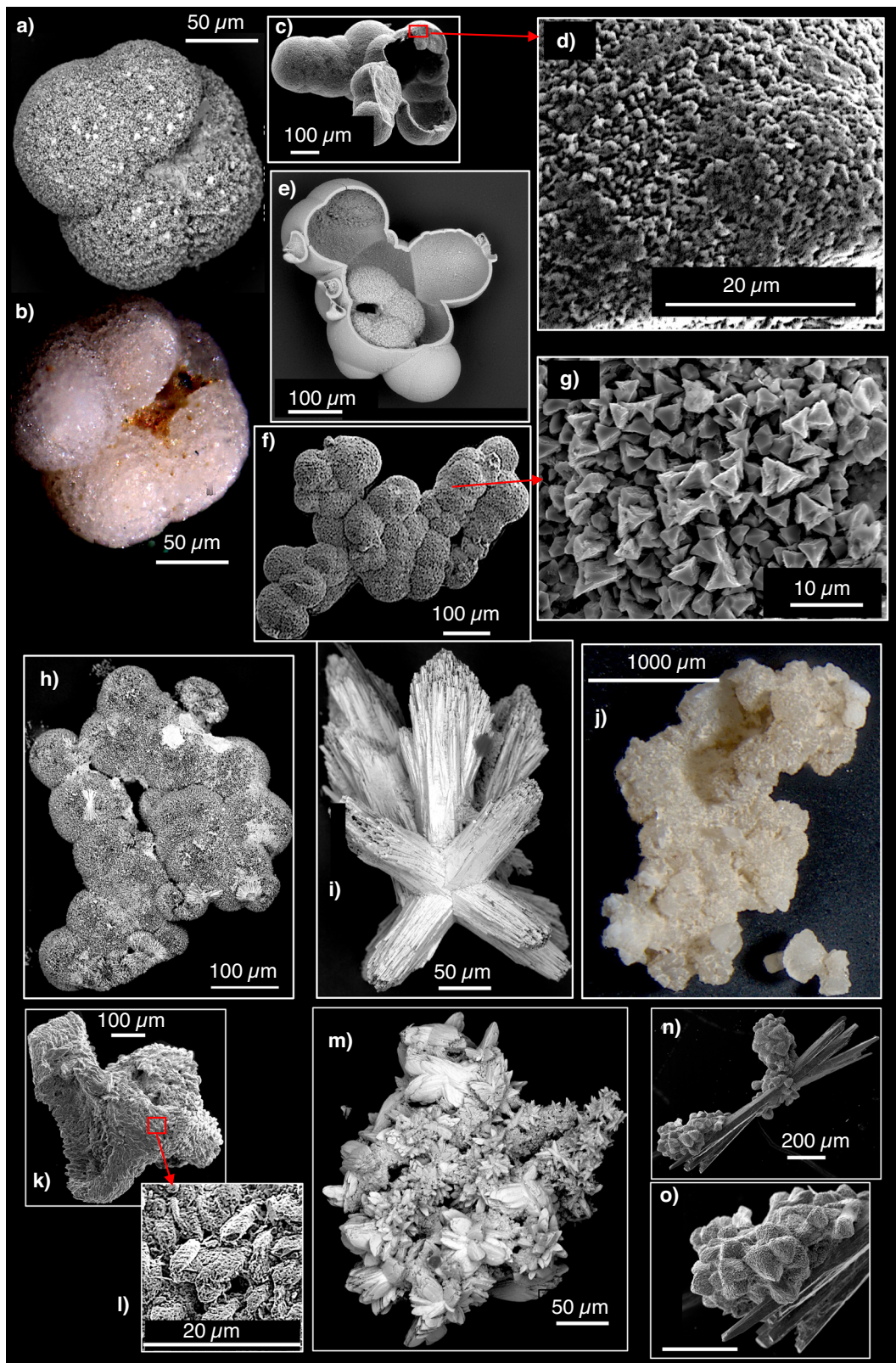


Fig. 3 Surface texture of heavily encrusted *N. pachyderma* tests and sedimentary authigenic crystals. **a, b** Brownish discolored overgrowth of tetrahedral calcite crystals. **c–e** Authigenic envelopes: **c–e** Microcrystalline envelope, **d** close-up of **(c)**, **e** *N. pachyderma* with porous overgrowth in envelope. **f, g** Tetrahedral envelope around juvenile planktonic foraminifera (**f**), **g** close-up of **(f)**. **h–o** Selection of authigenic crystals. **h** Authigenic spheres of needle-like calcite crystals, likely pseudomorphs after high Mg-calcite. **i** Wheat-sheaf-like bundles of needle-like crystals, likely pseudomorphs after high Mg-calcite. **j** Crystal crust. **k, l** Aggregate of small crystals. **l** Close-up image of **(k)**. **m** Authigenic crystals resembling glendonite. **n, o** Cluster of crystals. Needle bundle is likely a pseudomorphosis after aragonite, the dumbbell-like clusters are pseudomorphs after high Mg-calcite. **b, j** Stacked Axio Zoom, **a, c–h, k–o** SEM images. **d** PS2185-6, **a–c, e–o** PS72/413-3. Core depth (cm) **a, b** 22.5, **c–g** 17.5, **h** 20.5, **i–o** 22.5.

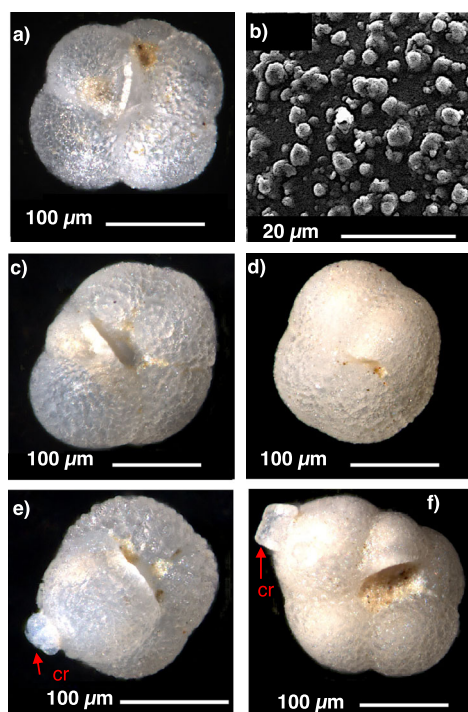


Fig. 4 Images on the classification of the preservation status of *Neogloboquadrina pachyderma*. **a** Pristine translucent PI₁ specimen. **b** Close-up view of primary shell showing smooth wall with low protuberances. **c, d** Specimens with no visible overgrowth PI₂. **c** Translucent-white specimen, **d** white specimen. **e, f** Specimen with visible overgrowth PI₃, both with distinct crystals, on translucent-white (**e**), and white shell (**f**). Specimen from core PS72/413-3. Core depth: **a, b** 6.5 cm; **c, d** 4.5 cm; **e, f** 11.5 cm. Stacked Axio Zoom images. cr = crystal.

Due to a slight brownish discoloration²² different from the other PI₂ shells, the ages between 18.5 and 23.5 cm are considered unreliable (see <https://www.pangaea.de/?q=doi:10.1594/PANGAEA.938246>).

At site PS2185, the ages of PI₃ shells resemble published conventional AMS ages on *N. pachyderma* from the box corer⁴, whereas PI₂ specimens below 10 cm, less affected by overgrowth, show distinctively younger ages (Fig. 5d and Supplementary Table 6). Below 20 cm, only PI₃ shells are found, and between 30 and 118 cm, a barren interval prevents any measurements. The structure of the radiocarbon chronology based on PI₃ specimens resemble those in a number of cores in the Arctic Ocean (Figs. 1 and 7).

The radiocarbon measurements of crystals of various morphologies reveal ages between >20 and 50 ¹⁴C ka, with the oldest ages obtained from large, the youngest from aggregates of small crystals (Fig. 5c, f). The ages of the small crystal aggregates are probably distorted by adhering sediments on the rough surface.

While the age of the idiomorphic crystals increases with depth, that of envelopes (without foraminifera) shows no relation to depth. Duplicate measurements on a broken yet single idiomorphic large crystal from the sediment surface at site PS72/404 (Fig. 1) reveal ages of 30.32 and 12.19 ka. This indicates that authigenic calcite forms discontinuously by repeated rather than a single precipitation event.

The occurrence of PI₁ specimen in grayish sediments (15–25 cm). In core PS72/413-3, the *N. pachyderma* shells between 15 and 25 cm core depth are almost exclusively whitish

to brownish with major overgrowth (Fig. 2b, sample documentation in <https://www.pangaea.de/?q=doi:10.1594/PANGAEA.938246>). Selecting PI₁ specimens from this section required to screen more than a hundred thousand shells of each sample. We assume that they originate from overlying brownish sediments, usually assigned to interstadial to interglacial sediments⁵¹, and were downcore displaced by burrowing organisms into the glacial grayish sediments. This interpretation is supported by: (1) the extreme rarity of this preservation state, (2) trace fossils in the form of brownish mottles in the grayish sediments, and (3) PI₁-radiocarbon age plateaus in these sediments.

Discussion

The process of authigenic carbonate precipitation in Arctic sediments. Previous studies have reported authigenic overgrowth on foraminifera shells primarily at seeps where methane is subsequently oxidized under anaerobic condition¹⁶. Methane as a classic source of old ¹⁴C in porewater and authigenic calcite is a well-known feature in Arctic shelves, and often linked to thawing permafrost^{52,53}. For the Arctic basin, hydrothermal seeps are numerous along the Gakkel Ridge⁵⁴, and can be suspected due to the many plutonic intrusions in the crustal area of the Mendeleev Ridge⁵⁵. However, while the ¹⁴C-depleted nature of PI₃ shells in principle supports methane as a carbon source, the very high $\delta^{13}\text{C}$ values recorded from our authigenic crystals are in sharp contrast to the extremely depleted $\delta^{13}\text{C}$ values recorded from DIC and from authigenic calcite precipitates in sediments close to the sea floor at methane emanation sites^{17,20–22,52}. Furthermore, sites PS2185 and PS72/413 are at a distance from the Gakkel Ridge and show no faunal evidence of hydrothermal activity at sites. Moreover, basin-wide no $\delta^{13}\text{C}$ or $\delta^{18}\text{O}$ anomalies indicative of hydrocarbon sources can be detected at the bottom water/sediment interface⁵⁶ and sediment cores examined reveal oxygen-rich pore waters in the uppermost 400 cm⁵⁷.

Degradation of labile organic matter would likewise result in depleted $\delta^{13}\text{C}$ signatures, while radiocarbon age offset would likely be less extreme than what we observe in our records. The central Arctic Ocean is an oligotrophic area with an extremely low mean labile organic carbon export production^{58–60}. Labile organic components of particulate organic carbon are only present in surface and near-surface sediments where they are immediately digested by benthos, whereas the majority is inert⁶¹. In porewater, dissolved carbon decreases with increasing sediment depth and labile components can only be detected in the uppermost 5 cm⁶⁰. In addition, the low central Arctic sedimentation rates do allow for extended oxygen exposure of near-surface sediment and bottom water where most labile organic carbon is immediately respired⁵⁹. This is reflected in low sedimentary organic carbon contents⁶² as in core PS72/413-3 (Fig. 8 and Supplementary Table 2). Porewater was not analyzed in the cores of this study but in core PS72/410-1 (Fig. 1) close to PS72/413-3, and PS72/248-6 on the Lomonosov Ridge porewater analyses reveal well-oxygenated pore waters with low TOC in the upper 400 cm (PS72/248-6)⁵⁷.

As Arctic Ocean deep-water has a modern to glacial $\delta^{13}\text{C}_{\text{DIC}}$ of ~1–1.5‰ Vienna Pee Dee Belemnite (VPDB)^{63,64}, lower than the observed $\delta^{13}\text{C}$ signature of PI₃ specimens, and any inorganic calcite precipitated from this water mass should reflect this in a 1:1 ratio, we rule out direct precipitation from bottom water. Calcite must therefore precipitate from porewater, possibly even close to the sediment surface, as indicated by filigree star-shaped crystals. Moreover, the huge variability in $\delta^{18}\text{O}$ values of especially large authigenic crystals, with lowest values equal to $\delta^{18}\text{O}$ values of Arctic glaciers or atmospheric precipitation⁶⁵,

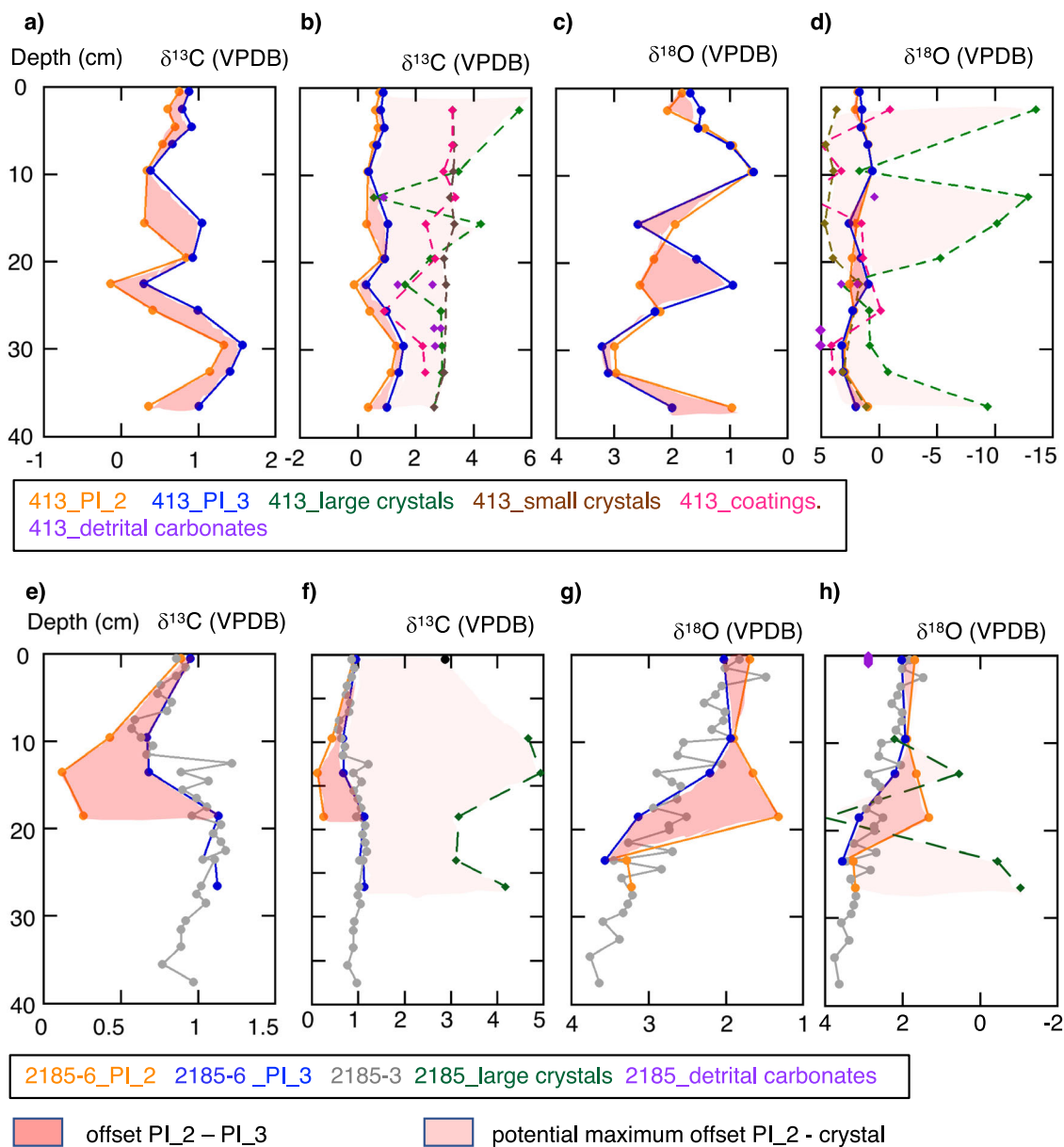


Fig. 5 Carbon and oxygen isotope values in the investigated cores. **a-d** PS72/413-3. **a, b** Carbon isotope values of *N. pachyderma* (**a**), and incl. crystals, envelopes and detrital carbonate (**b**). **c, d** Oxygen isotope values of *N. pachyderma* (**c**), and incl. crystals, envelope and detrital carbonate (**d**). **e-h** PS2185-6/3. **e, f** Carbon isotope values of *N. pachyderma* this study and Nørgaard-Pedersen⁴ (**e**), and incl. crystals (**f**). **g, h** Oxygen isotope values of *N. pachyderma* this study and Nørgaard-Pedersen⁴ (**g**), and incl. crystals (**h**).

suggest a periodically low saline crystallization fluid for the large, thus slow-growing crystals. Carbon and oxygen analyses of epifaunal (*Cibicidoides wuellerstorfi*) and shallow-infaunal (*Cassidulina neoteretis*) dwelling in bottom (*C. wuellerstorfi*) respectively porewater (*C. neoteretis*), show especially for PI_3 *C. neoteretis* a strong positive $\delta^{13}\text{C}$ but negligible $\delta^{18}\text{O}$ -offset (Supplementary Table 3). As these foraminifers have precipitated their shells in these habitats, a continuous freshwater influence at the sediment-water interface or in the respective porewater can be ruled out.

In core PS72/413-3, the occurrence of thick overgrowth (major overgrowth Fig. 6a) and sedimentary authigenic calcite crusts peak in the pink-white ice-rafted sediments below 27 cm (Fig. 9). Similarly, colored ice-rafted calcite clasts distributed throughout both cores fall into the carbon and oxygen isotope range of crystals from the same sediment depth (Fig. 5). As the high radiocarbon age and carbon isotope values of crystals indicate an

old and ^{13}C -enriched carbon source, we assume that ice-rafted calcite flour serves as a reservoir for authigenic calcite. Nørgaard-Pedersen reported authigenic carbonates in the coarse-size fraction of foraminifera-poor, clay to silt-sized ice-rafted Paleozoic Mg-calcite flour-rich (thereafter calcite flour) glacial sediments from Northern Greenland-Northern Canada, in sediment cores from the Gakkel Ridge (PS2166) and Morris Jesup Rise (PS2200)⁶⁶ (Fig. 1). He also considers increased calcite flour supply as causal for the formation of large authigenic calcites. Distributed by bioturbation throughout the sediments, or dissolved in porewater, calcite flour may support a persisting, pore/bottom water buffer capacity for more or less extended times of CO_2 storage⁶⁷⁻⁶⁹. This process is comparable to the hard water effect, which results from the dissolution of limestone grounds in aquatic systems¹⁰. During times with corrosive bottom/porewater or by, in this oligotrophic environment, only facultative, organic matter degradation, calcite flour and variable

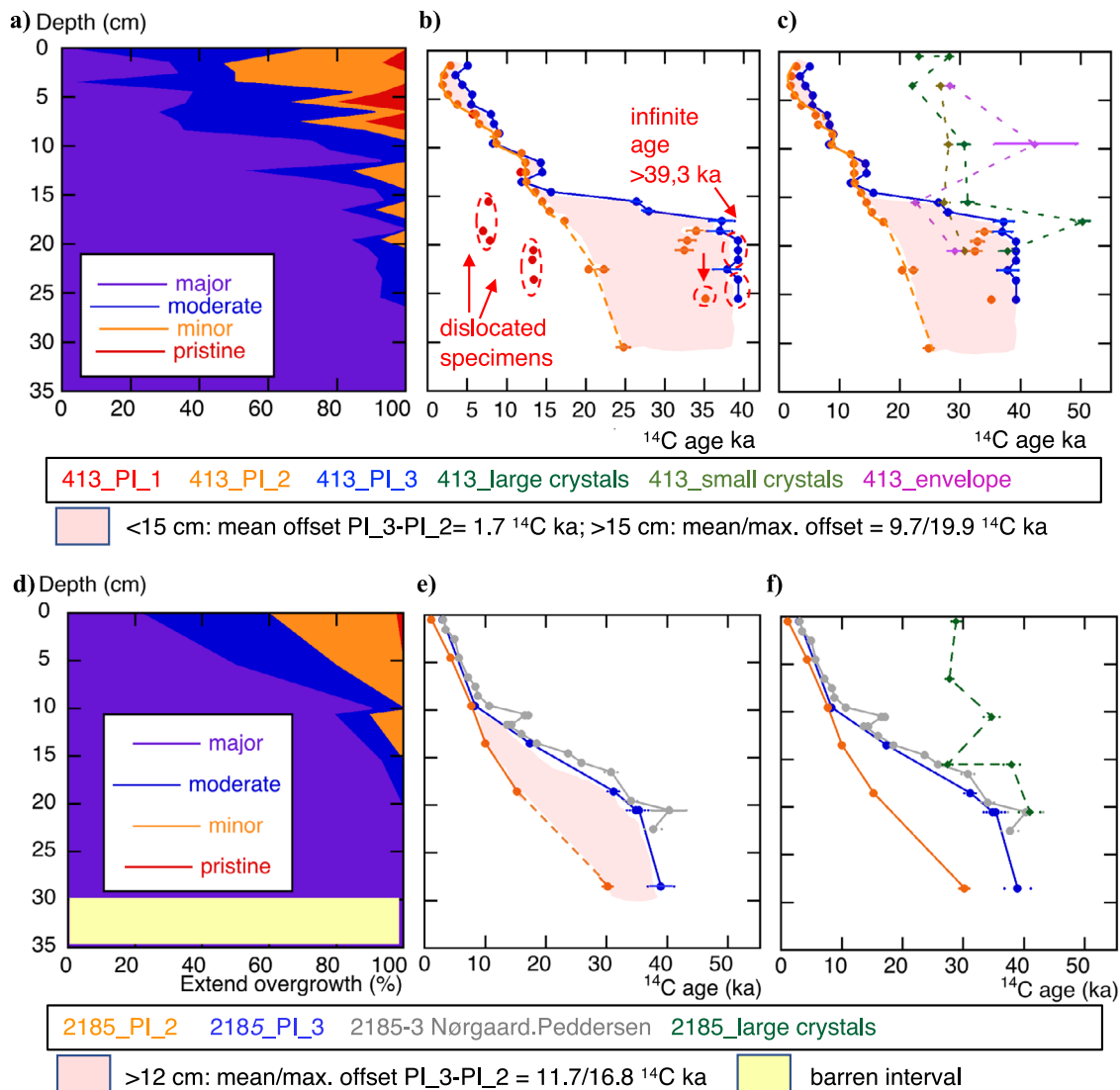


Fig. 6 Extent of overgrowth and radiocarbon ages of the respective preservation index categories. **a–c** PS72/413-3. **a** Mean relative estimates of overgrowth (no, minor, moderate, major). **b, c** ^{14}C age vs depth of PI₁₋₃ shells (**b**), and incl. crystals (**c**). **d–f** PS2185-6/3. **d** Mean relative estimates of overgrowth (no, minor, moderate, major). **e, f** ^{14}C age vs depth of PI₁₋₃ shells (**e**), and incl. crystals (**f**). Please note that PI-measurements (**b, c** and **e, f**) are based on stereomicroscope investigations, mean relative estimates (**a** and **d**) additionally on SEM analysis. However, major overgrowth was usually noticed on discolored brownish specimens, that were not measured, thus are not included in PI₃ results. Error bars represent $\pm 2\sigma$ analytical uncertainty.

amounts of biogenic carbonates may dissolve. At a later date, with well-ventilated bottom and porewater, high sedimentary clay contents^{70,71} mediated by microbial communities^{72,73}, sulfate or iron⁶⁸ reduction eventually lead to increased porewater alkalinity and pH resulting in a precipitation of calcite⁷¹.

An alternative mechanism of authigenic carbonate formation has been recently described by Rogov et al.⁷⁴. Under favorable melting and freezing conditions combined with porewater chemistry changes, carbonates may grow by cryometamorphism in free pore spaces of permafrost on the shallow Siberian shelves. Such geochemical processes could also lead to the precipitation of calcites in the deep Arctic Ocean.

Especially, the oxygen and carbon isotope ratios of the crystals are extremely variable, both downcore and even within one crystal. Thus, besides calcite flour, regarded as a major source of authigenic calcite precipitation, variable other sources are needed to explain especially the sometimes extremely depleted $\delta^{18}\text{O}$ values of crystals. The oldest radiocarbon age we could retrieve for PI₂ specimens was from core PS2185-6 at 25 cm; below this depth, sediments are barren in microfossils and coeval with a

period when the Arctic Ocean was flooded with freshwater⁴⁹. In core PS72/410-1 (Fig. 1), which is adjacent to PS72/413-3, sedimentary authigenic neodymium isotopes also indicate increased freshwater inputs at the same time⁷⁵. At present neither models nor porewater data aid to understand this persisting precipitation process that, according to the existing data, can be explained neither by the degradation of labile organic material nor by increased methane concentrations. However, in the central Arctic Ocean, sedimentation rates are extremely low, and during glacial times periods with high sediment flux likely alternated with times of diminished sedimentation. Any porewater chemistry thus likely altered distinctly over time. Combined porewater and lithological investigations, potentially supported by experimental set-ups, will be needed to unravel the formation of the ubiquitous authigenic calcites in the central Arctic Ocean.

Can foraminiferal shells be cleaned from overgrowth? Foraminifera shells are not solid calcite but they contain organic linings deposited either as sheets for the nucleation of calcite

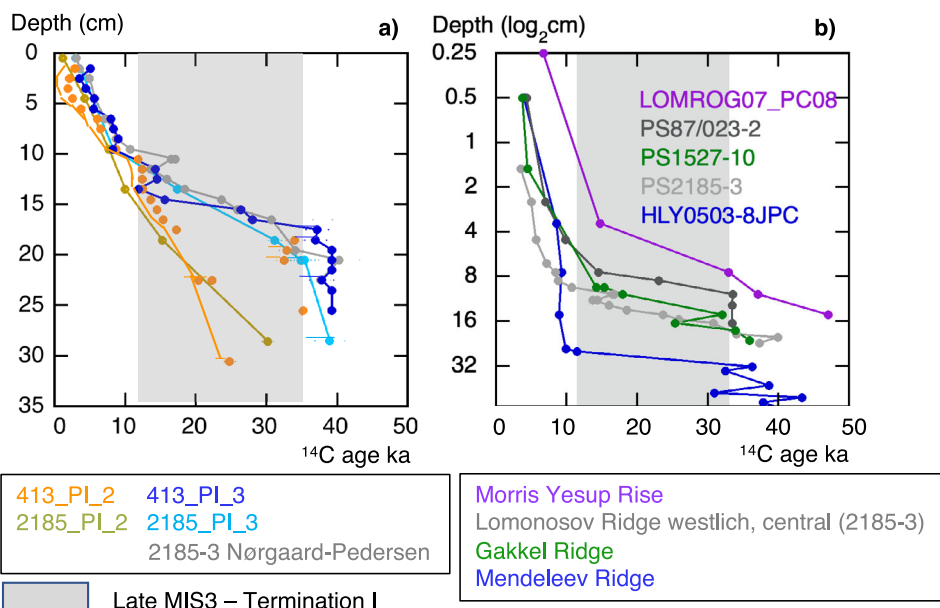


Fig. 7 Comparative radiocarbon ages and their implication for the assumption of missing late glacial sediments. **a** PL₂ and PL₃ specimens in the analyzed cores vs published data. **b** Exemplified radiocarbon records from the Mendeleev, Lomonosov Ridge and Morris Yesup Rise (see also Supplementary Fig. 1). See the almost linear age development downcore of PL₂ specimens and the distinct age jump of PL₃ specimen and published records in glacial sediments.

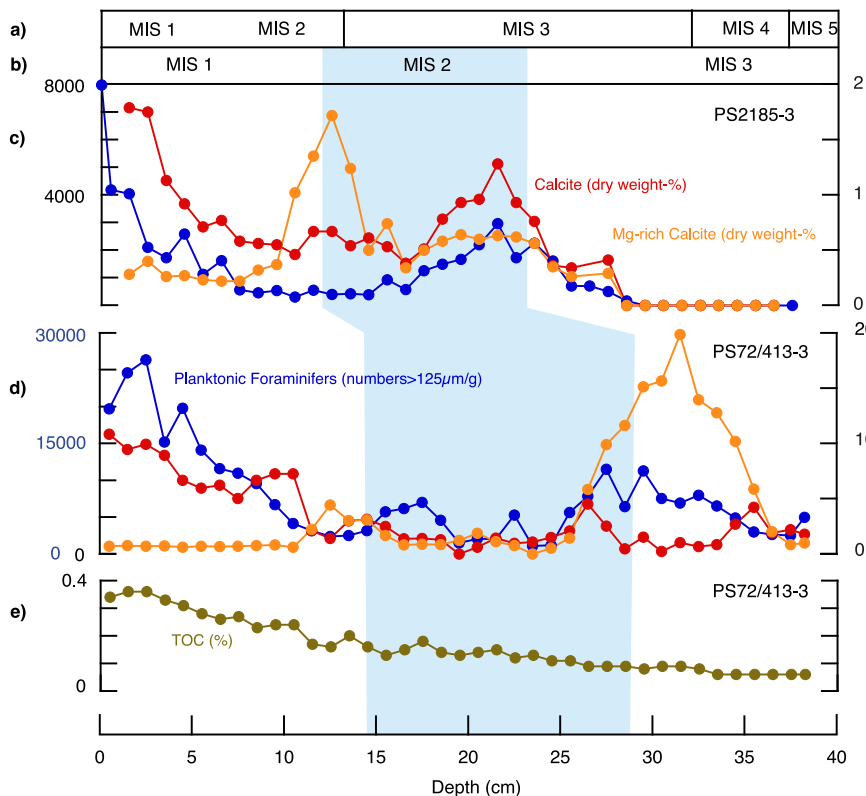


Fig. 8 Chronostratigraphy and sediment characteristics cores PS72/413-3 and PS2185-3⁶⁶. **a** Published stratigraphy of core PS2185-3. **b** Chronostratigraphic interpretation based on ¹⁴C ages of PL₂, non-calibrated and without reservoir correction (see Fig. 6b, e). **c, d** Relative abundance of carbonates quantified from X-ray diffraction analyses of bulk sediments¹⁰⁰, and planktonic foraminifera numbers for cores **c** 2185-3⁶⁶ and **d** PS72/413-3⁹⁴. **e** Total organic carbon PS72/413-3.

precipitation and shell protection³³, or surrounding single or groups of interlocking calcite mesocrystals⁷⁶ (Fig. 10).

Whereas the biologically precipitated pristine shell in cross-section appears rather solid, and especially in the secondary

calcite crust mesocrystals are radially aligned (Fig. 10a), its porous structure and multiple organic/mesocrystal boundaries make it vulnerable to dissolution. Pores enlarge and mesocrystals corrode especially where in contact with organic sheets (Fig. 10b, c).

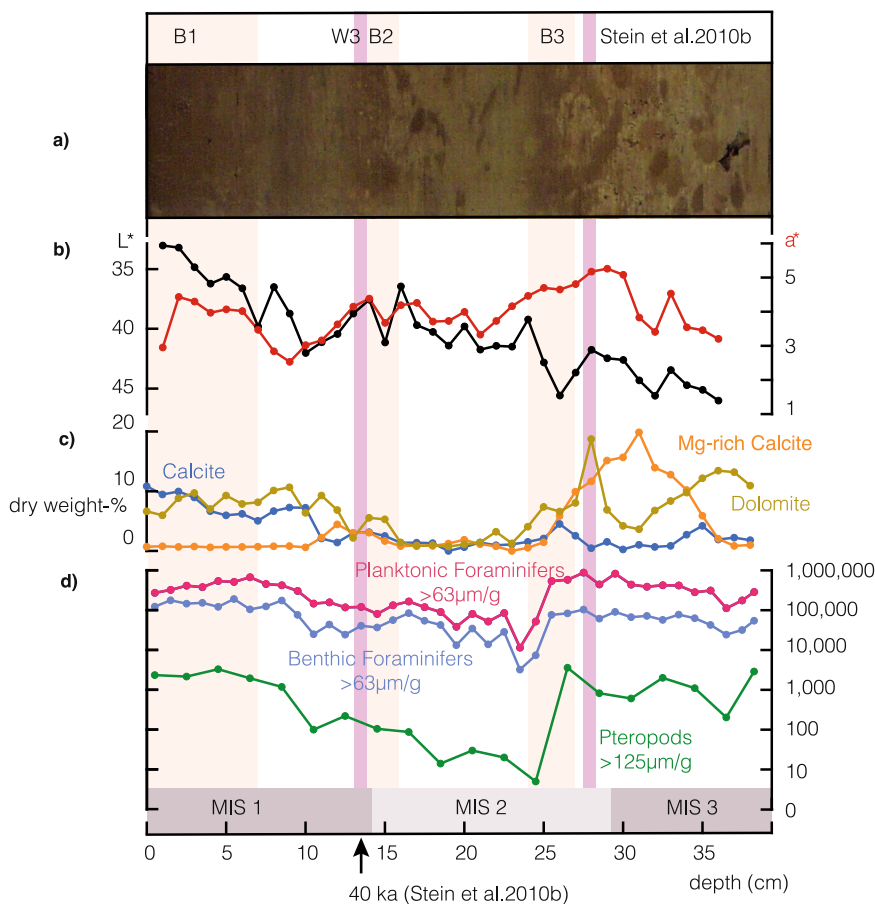


Fig. 9 Sediment characteristics core PS72/413-3. **a** Linescan image with published chronostratigraphic interpretation⁵¹. **b** Lightness L^* and green-red color space a^* . **c** Relative abundance of carbonates quantified from X-ray diffraction analyses of bulk sediments⁹⁴. **d** Concentrations of planktonic and benthic foraminiferal and pteropod shells. MIS placement this study.

When the pH rises and authigenic calcite precipitates, it also penetrates into these cavities, masking the original radial mesocrystal alignment (Fig. 10d, e).

The common way to remove authigenic overgrowth is to expose the shells to a weak acid (leaching) to hydrolyze the contamination prior to the AMS measurement of the remaining shells⁷⁷. Since in our samples the shells were exposed to a repeated interplay between dissolution and authigenic calcite precipitation, the porosity of the biogenic calcite far exceeds that of the authigenic calcite. Consequently, leaching would mainly affect biogenic but not authigenic calcite.

Impact on Arctic Ocean radiocarbon chronology and paleoceanographic reconstructions. At PS2185, one of the key sites in the Central Arctic Ocean, the PI_3 ages and stable oxygen and carbon isotopes are comparable to published records⁴ indicating that predominately PI_3 specimens were previously analyzed (Figs. 3c and 4). An almost instantaneous age shift on the order of 10–15 ka at this site in the PI_3 record, also observed at other Central Arctic Ocean sites (Fig. 7 and Supplementary Fig. 1), has been interpreted as an apparent absence of MIS 2 sediments^{78,79}, or a mixture of MIS1 and MIS 3 sediments⁷⁹. Our results suggest a more uniform age increase downcore derived from PI_2 specimens, indicating that previous interpretations might have suffered from age biases. We thus propose that the chronology for the past 30 ka should be critically re-evaluated (see methods). Measuring shells (foraminifera, ostracoda, pteropoda, bivalves, otoliths⁷⁹) with a distinct brownish discoloration,

indicating the incorporation of exogenous components, should be avoided.

Consequently, previous interpretations of sediment core records need careful revisions. Apart from a different chronology of lithostratigraphic units that are useful for stratigraphic correlation at the Mendeleev Ridge (methods), our results may have a tremendous impact on paleoceanographic interpretations. If the presence of MIS 2 sediments is confirmed at many sites, the last glaciation may be studied at a low resolution in the Central Arctic Ocean. Since these sediments comprise a maximum of planktonic foraminifera and some biogenic calcite at the base of MIS 2 (Figs. 8d and 9), a permanent thick sea-ice cover during the entire MIS 2²⁷ can be excluded. The proposed high productive zone with seasonally open water conditions up to 84–85°N²⁷ may thus have extended at least to the Lomonosov Ridge. The relatively high abundances of *N. pachyderma* in core PS72/413-3 at the southern Mendeleev Ridge support a relatively high production during seasonally ice-free conditions in early MIS 2.

Final remarks and recommendations. The majority of overgrowth observed in our samples consists of a more or less thick homogenous coating of authigenic calcite which may easily be overlooked on the coarse secondary calcite crust of *N. pachyderma* (Fig. 2i, j). Only by careful inspection at high magnification under the stereomicroscope, such overgrowth can be noticed, but early tiny overgrowth may still be overlooked. Merely the investigation of foraminiferal shells from small sample splits under the stereomicroscope and SEM reveals information on the extent of overgrowth in the respective sample.

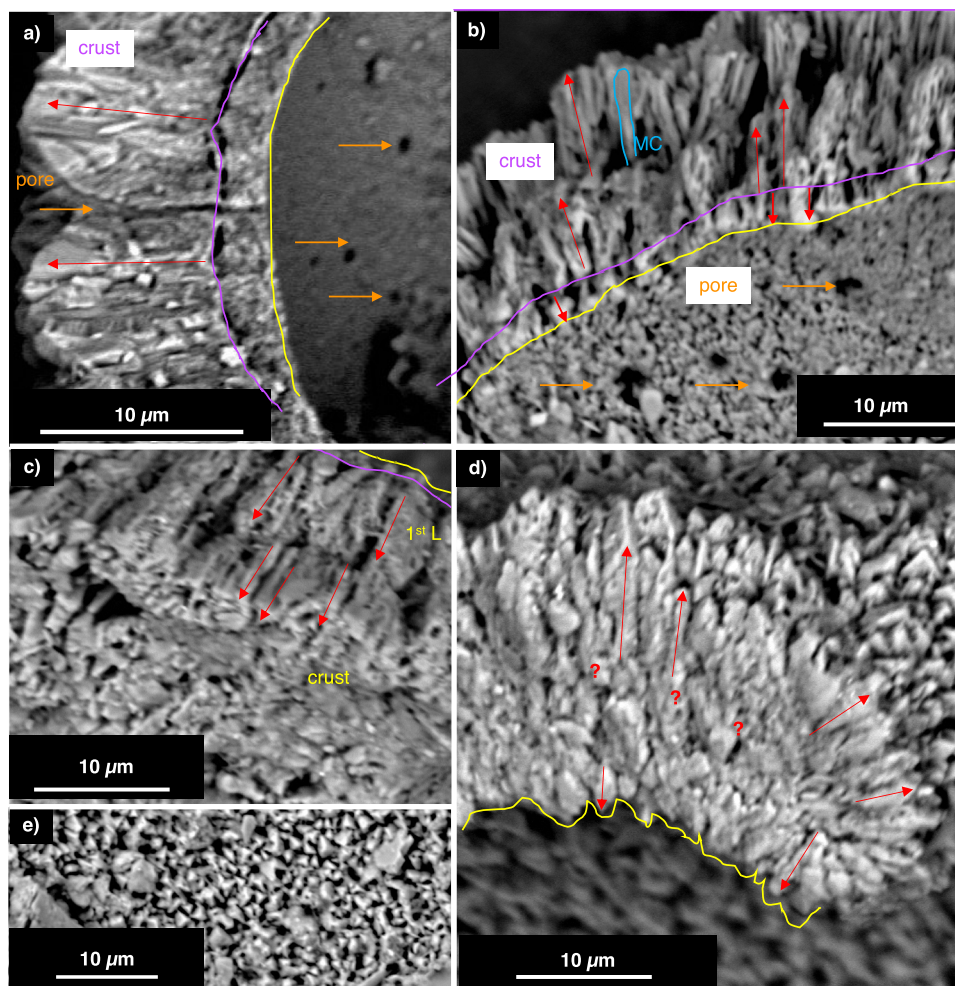


Fig. 10 Diagenetic alteration of *N. pachyderma* shells. **a** Pristine shell with secondary calcite crust and smooth shell interior. **b, c** Shell affected by initial dissolution, showing widened pores and especially at the border of previously existing organic sheets large cavities. **d, e** Shell with authigenic calcite on the exterior and interior (**e**) surface and penetrating the shell, hereby destroying the original shell structure (**d**), see also the rough interior shell surface (yellow line). PS2185-6. Core depth (cm): **a–c, d, e** 10 cm. Lines indicate the original position of the inner shell surface (yellow), the presumed border between primary shell and secondary crust (purple). Red arrows = growth direction of mesocrystals. Blue line highlights single mesocrystal.

The unknown variability of sea-ice extent, upwelling and ocean-atmosphere exchange complicates an unambiguous calibration of radiocarbon ages, particularly in the Arctic Ocean⁸⁰. Overgrowth now adds an omnipresent additional complication to obtaining accurate radiocarbon chronologies. Besides authigenic calcite, initial dissolution is observed on some shells of PS2185-6 (Fig. 10d) and may here also contribute to the altered shell-based proxies^{10,12–14,25,43–45} of PI_3 specimen.

Furthermore, when assessing glacial radiocarbon ages, one has to keep in mind that planktonic foraminifera require primary production for nutrition. Under a much thicker ice cover, they could only reproduce and be ultimately deposited when ice thickness was episodically reduced. Coupled with very low sedimentation rates and intensive bioturbation, each MIS 2 radiocarbon age measured on PI_2 specimens will reflect one or several of such events. Deduced from the crystals, an old carbon source eventually admixed with variable small proportions of dissolved biogenic aragonite or calcite contributes to the precipitates. This makes the application of correction factors for overgrowth impossible.

This study highlights challenges afflicted with our present-day shell-based work. The commonly assumed chronology of Arctic Ocean sediments may deviate by more than 10,000 years from the

true chronology in critical parts of the last deglaciation and thus impede the final resolution of ocean condition reconstruction controversies^{49,81}. The PI_2 specimen ages and isotope values reported here are reasonable for the Holocene and distinctively improved for the glacial. However, only specimens screened beforehand under the SEM, confirmed ideally to be free of overgrowth and dissolution, will enable credible radiocarbon and proxy measurements of glacial samples. These measurements are the cornerstones of Arctic chronology, paleoceanographic reconstructions and, ultimately, climate models.

Materials and methods

The surface samples and sediment cores analyzed in this study were retrieved with the RV Polarstern from sites and with devices as listed in Supplementary Table 1. X-ray images do not give evidence for hiatuses in sedimentary records. For both cores, numerous supplementary information to this paper can be retrieved from <https://doi.org/10.1594/PANGAEA.938246>.

Lithostratigraphy. The sedimentary sequence of core PS72/413-3 consists of alternating brown and gray beds interbedded with whitish to pink layers or clasts (Fig. 10a). Distinct mottling indicates that in particular brown beds are extensively bioturbated. As it has been previously proposed by Polyak et al.⁸², Stein et al.⁵¹ labeled the brown beds downcore and identified brown beds B1–B3 in core PS72/413. This lithostratigraphy has been used for stratigraphic correlation across the Mendeleev Ridge⁵¹. In the Mendeleev Ridge area, the brown beds are usually

assigned to interstadials or interglacials, gray sediments to stadials or glacials, based predominately on the variability of calcareous foraminifera^{6,83}. Pink to white sediments are rich in detrital dolomite and reflect massive discharge of icebergs from the Laurentide ice sheet^{6,51,75,78,84}. The lithology of core PS72/413-3 is difficult to tie into the principal lithostratigraphy at the Mendeleev Ridge based on the new analytical data. The characteristic combination of low lightness L* and high green-red color space values a* in the brown beds⁶ is only seen in B1 and B2 (Fig. 10a, b). Calcite is only abundant in the topmost 10 cm (Fig. 10c), whereas calcareous microfossils (planktonic and benthic foraminifera, pteropods) are consistently abundant throughout the core (Fig. 10d, note logarithmic scale) being slightly more abundant at the top and base of the core. This pattern differs from those previously observed in cores from the Mendeleev Ridge area where brownish sediments contain considerably higher abundances of calcareous microfossils than grayish sediments⁶. Finally, the white layer W3 is not reflected in increased dolomite contents. Therefore, we generally adopt the lithostratigraphic interpretation of Stein et al.⁵¹ with slight revisions. Color reflectance data indicate a much thicker brown bed B1. The stratigraphic marker horizon W3 which is linked to brown bed B2 is difficult to identify because it thins out from the Amerasian Basin to the Makarov Basin⁵¹. Few pink-white clasts have been observed at ca. 14 cm but these are not associated with high dolomite contents. The peak abundance of dolomite at ca. 28 cm may rather be linked to W3 but a distinct layer is not observed. Since pink-white clasts may be enriched in a horizon at the base of B3 in sediment cores with relatively high sedimentation rates⁵¹, this peak is rather linked to a different white layer. Sediment layers with the highest Mg-rich calcite contents (Figs. 8c, d and 10c) are possibly coeval with those at sites located off northern Greenland⁸⁵. Here, grain size-specific X-ray diffraction (XRD) measurements in cores from site PS2200 show the highest concentrations of high Mg-calcite in the finest sediments, especially in the clay fraction⁸⁵. These sediment layers are derived from iceberg, sea-ice and ocean current transport of glacial rock flour eroded in northern Greenland based on evidence from sediment cores located near the northern mouth of Nares Strait^{86,87}. Therefore, we assume that most of the fine-grained calcareous detritus in core PS72/413-3 was also derived from glacial rock flour as is observed in neighboring cores⁸⁸.

Chronostratigraphy of sediment cores PS72/413-3 and PS2185-6. Stein et al.⁵¹ discussed published age models for sediment cores at the Mendeleev Ridge, which are rather tentative beyond the range of radiocarbon dating. Thus, brown beds B1 and B2 are consistently dated to the Holocene and late MIS 3, respectively^{6,51,75}, while B3 has been assigned either to MIS 4/5^{6,75,78,83} or 3/4^{75,89} (Fig. 10a). These age models have been transferred by lithostratigraphic correlation to PS72/413-3 suggesting a much older age of ca. 40 ka at ca. 12 cm⁵¹ than the chronology based on PI_2 and PI_3 specimens. The new uncalibrated radiocarbon chronology confirms the age of B1 but arrives at much younger ages for the older brown beds. Both brown beds are dated to MIS 2 based on radiocarbon ages of PI_2 specimens, while the ages from PI_3 specimens support the presence of a hiatus, encompassing MIS 2. Comparable discrepancies are observed at site PS2185-6 when the new radiocarbon chronology of PS2185-6 is compared with the published record of the box corer PS2185-3^{4,27,90} (Fig. 3). The stack of Spielhagen et al.⁹¹ was not used because we could not find any conclusive evidence for their correlation. Both cores were correlated one-to-one without any depth adjustments. The consistent offset between the chronology proposed by standard AMS¹⁴C ages and PI_3 specimens, and that based on selected PI_2 specimens call for a re-evaluation of Arctic chronostratigraphy in the range of radiocarbon chronologies.

X-ray diffraction. XRD pattern analyses have been done in the laboratories of the research group Crystallography and Geomaterials (University of Bremen, FB05 Geosciences). Dried bulk samples have been grounded to a fine powder (<20 µm particle size) and prepared with the Philips backloading system. A thorough preparation commonly increases reproducibility of the results; however, the standard deviation given by Moore and Reynolds⁹² of ±5% can be considered as a general guideline for mineral groups with >20% clay fraction. In addition, the determination of well-crystallized minerals like quartz, calcite or aragonite can be done with better standard deviations (±1–3%)^{93,94}. The X-ray diffractograms have been measured on a Philips X'Pert Pro multipurpose diffractometer equipped with a Cu-tube (k_{α} 1.541, 45 kV, 40 mA), a fixed divergence slit of ¼°, a 16 samples changer, a secondary Ni filter and the X'Celerator detector system. The measurements have been done as a continuous scan from 3 to 85° 2θ, with a calculated step size of 0.016° 2θ (calculated time per step was 50 s). Mineral identification has been done by means of the Philips software X'Pert HighScore™ and identification of sheet silicates has been done with the freely available Apple MacIntosh XRD interpretation software MacDiff 4.25⁹⁵. This was followed by full quantification of mineral assemblages of the bulk fraction via the QUAX full pattern method⁹⁴.

Micropaleontological work. One-centimeter-thick samples were taken continuously from core PS72/413-3, and at 5-cm intervals from core PS2185-6. All samples were freeze-dried, and their weight was determined (mean freeze-dried sample weight is 77 and 104 g for cores PS72/413-3 and PS2185-6, respectively) (Supplementary Tables 2 and 6). Surface sediments from multiple corer (MUC) casts were treated with a volume equivalent Rose Bengal/Ethanol (96%) mixture

(1 g Rose Bengal per L Ethanol), not freeze-dried, and no weight was determined. All samples were washed with tap water over a 63 µm sieve and oven dried (50 °C). The residue was dry sieved over a 125 µm sieve. For core PS72/413-3 planktonic and benthic foraminiferal numbers were calculated from sample splits (micro-splitter) (Supplementary Table 2). Isotope and AMS analyzes were performed on the size fraction >125 to <250 µm. Except for cores PS72/413-3 and PS2185-6, only the surface sample of MUCs was qualitatively inspected for overgrowth on foraminifera and sedimentary authigenic crystals. In plots, all data are plotted as sample mid depth (0–1 cm = 0.5 cm).

All stereomicroscope images are stacked digital images taken under a Zeiss Axio Zoom.V16 microscope equipped with ×16/16 Br. foc. oculars and the objectives PlanNeoFluar Z ×1.0 (numerical aperture 0.25, FWD 56 mm, magnification ×11...×179 with eyepieces PL ×16/16; object field in mm 23...1.4), and Apo Z ×1.5 (numerical aperture 0.37, magnification ×10.5...×168 with eyepieces PL ×16/16; object field in mm 15...0.95). The numerical aperture is 0.25, and the microscope uses the ZEISS ZEN 2.3 (blue edition) imaging software. Images were taken with a ZEISS AxioCam 506 color microscope camera. Each measured sample was documented beforehand by one to several images (see documentary of samples under <https://www.pangaea.de/?q=doi:10.1594/PANGAEA.938246>).

SEM images and EDS measurements are performed by means of a JEOL JSM-IT100 InTouchScope™ Scanning Electron Microscope. Samples mounted on aluminum stubs using conductive double-sided carbon tape are analyzed without conductive coating in low vacuum mode. Elemental concentrations of samples are the average of ten EDS point measurements, performed at slightly different positions on the sample with an integration time of 45 s per measurement. Due to the roughness of the sample surface, the angle between the sample surface and the EDS detector is not constant (like on a flat polished surface). Due to the topography of the sample, the elemental concentrations determined show a relatively high standard deviation. However, the qualitative differences between different types of samples (structures) are clearly revealed. The documentation of foraminiferal shells is performed on uncoated specimens, only in core PS72/413-3 the specimens from 1.5 to 10.5 cm depths were coated with charcoal in the 306 Vacuum Coater with Turbomolecular Pumping System of Edwards.

To document the degree of overgrowth in both cores downcore, from >125 µm to <2 mm size fraction all *N. pachyderma* specimens of sample splits containing 10–30 specimens of each sample were glued on SEM stubs and documented (see <https://www.pangaea.de/?q=doi:10.1594/PANGAEA.938246>). Hereby, a relative qualitative assessment of the overgrowth on *N. pachyderma* shells is provided by combined Axio Zoom and SEM images (see <https://www.pangaea.de/?q=doi:10.1594/PANGAEA.938246>).

Radiocarbon measurements. For PI_1 measurements, 20 and 80 specimens were picked from the whole sample >125 to 250 µm of core PS72/413-3, and split into subsamples of 20–30 specimens for replicate measurements. For PI_2 and PI_3 measurements, 60–80 specimens (min 20 if abundance was too low) collected from sample splits of 3.13–6.25%, were selected for each measurement. At site PS72/413-3, two depths containing >800 specimens of PI_2 (18.5 cm) and PI_3 (17.5 cm) were picked for comparison with measurements of smaller samples from the same depth (Supplementary Tables 4 and 5). For the ages of core PS2185-3 between 1000 and 2000 specimens were picked from the 125–250 µm fraction^{4,93}. From all *N. pachyderma* isolated, the best-preserved individuals were used for radiocarbon and spare individuals for isotope measurements. The majority of radiocarbon measurements were performed with the MICADAS at the Alfred Wegener Institute (AWI), unless otherwise noted. Equipped for gas measurements of samples containing 20–100 µg C^{29,30} it is possible to obtain ¹⁴C ages on only 20–60 *N. pachyderma* specimens in contrast to approximately 1000 specimens required for standard AMS analyses. Radiocarbon analysis was conducted following standard operating procedures as detailed by Mollenhauer et al.⁹⁶. Briefly, 0.2–0.3 g of foraminifera shells were filled in septum sealed vials and processed using the carbonate handling system. The sample vials were flushed for 5 min with 70 mL/min ultra-pure helium (99.99% He) to remove atmospheric CO₂, and afterward 200 µL of phosphoric acid (≥85%, Fluka 30417) was added. The hydrolyzation of carbonates to CO₂ took place over ~30 min at 70 °C. Following complete hydrolyzation, CO₂ was flushed from the vials by a He flow. Residual moisture was removed from the gas stream over a phosphorus pentoxide trap and CO₂ was concentrated on the zeolite trap of the Gas Interface System. Following thermal expansion of the CO₂ from the zeolite trap, the gas was manometrically quantified and He was added to obtain a gas mixture of ~5% CO₂ in He. The gas mixture was subsequently fed to the MICADAS gas ion source. The radiocarbon data were normalized against Oxalic Acid II standard gas (CO₂ produced from NIST Oxalic Acid II, NIST SRM4990C) and blank correction was performed against size-matched blank foraminifera (pre-Eemian age carbonate fraction from GeoB3316-1, 521–541 cm, >150 µm) processed alongside the samples.

Oxygen and carbon isotope measurements. Stable isotopes were measured with the stable isotope ratio mass spectrometer Thermo Fisher Scientific MAT253 with an automated Kiel IV device at AWI. As this instrument performs best with 30–60 µg carbonate, 20–30 *N. pachyderma* or a respective number/weight of crystals were used for each measurement. External reproducibility of δ¹³C and δ¹⁸O measurements based on an internal laboratory standard (Jurassic limestone

and Solnhofen limestone) measured over a 1-year period together with samples was better than 0.04‰ VPDB for ^{13}C and 0.08‰ VPDB for ^{18}O . Isotope data was converted to the delta notation⁹⁷. All carbonate isotope data are given in per mil (‰) relative to the VPDB standard.

Data availability

The datasets used and generated during the current study are available in the PANGAEA data repository, <https://www.pangaea.de/?q=doi:10.1594/PANGAEA.938246>, where the previously published datasets are also linked and referenced.

Received: 18 May 2022; Accepted: 12 April 2023;

Published online: 22 April 2023

References

- Dai, A., Luo, D., Song, M. & Liu, J. Arctic amplification is caused by sea-ice loss under increasing CO₂. *Nat. Commun.* **10**, 121 (2019).
- Lohmann, G. et al. Challenges in the paleoclimatic evolution of the Arctic and subarctic Pacific since the Last Glacial period—the Sino–German Pacific–Arctic Experiment (SiGePAX). *Challenges* **10**, 13 (2019).
- Docquier, D. & Koenigk, T. Observation-based selection of climate models projects Arctic ice-free summers around 2035. *Commun. Earth Environ.* **2**, 144 (2021).
- Nørgaard-Pedersen, N., Spielhagen, R. F., Thiede, J. & Kassens, H. Central Arctic surface ocean environment during the past 80,000 years. *Paleoceanography* **13**, 193–204 (1998).
- Hillaire-Marcel, C., de Vernal, A., Polyak, L. & Darby, D. Size-dependent isotopic composition of planktic foraminifers from Chukchi Sea vs. NW Atlantic sediments—implications for the Holocene paleoceanography of the western Arctic. *Quat. Sci. Rev.* **23**, 245–260 (2004).
- Adler, R. E. et al. Sediment record from the western Arctic Ocean with an improved Late Quaternary age resolution: HOTRAX core HLY0503-8JPC, Mendeleev Ridge. *Glob. Planet. Change* **68**, 18–29 (2009).
- Poore, R. Z., Osterman, L., Curry, W. B. & Phillips, R. L. Late Pleistocene and Holocene meltwater events in the western Arctic Ocean. *Geology* **27**, 759–762 (1999).
- Cronin, T. M. et al. Deep Arctic Ocean warming during the last glacial cycle. *Nat. Geosci.* **5**, 631–634 (2012).
- Farmer, J. R. et al. Arctic Ocean stratification set by sea level and freshwater inputs since the last ice age. *Nat. Geosci.* **14**, 684–689 (2021).
- Douka, K., Higham, T. F. G. & Hedges, R. E. M. Radiocarbon dating of shell carbonates: old problems and new solutions. *Munibe Suplemento* **31**, 18–27 (2010).
- Skinner, L. & Bard, E. Radiocarbon as a dating tool and tracer in paleoceanography. *Rev. Geophys.* **60**, e2020RG000720 (2022).
- Sexton, P. F., Wilson, P. A. & Pearson, P. N. Microstructural and geochemical perspectives on planktic foraminiferal preservation: “Glassy” versus “Frosty”. *Geochem. Geophys. Geosyst.* **7**, Q12P19 (2006).
- Regenberg, M., Nürnberg, D., Schönfeld, J. & Reichert, G. J. Early diagenetic overprint in Caribbean sediment cores and its effect on the geochemical composition of planktonic foraminifera. *Biogeosciences* **4**, 957–973 (2007).
- Douka, K., Hedges, R. & Higham, T. Improved AMS ^{14}C dating of shell carbonates using high-precision X-ray diffraction and a novel density separation protocol (CarDS). *Radiocarbon* **52**, 735–751 (2010).
- Wenzhöfer, F. et al. Calcite dissolution driven by benthic mineralization in the deep-sea: in situ measurements of Ca²⁺, pH, pCO₂ and O₂. *Geochim. Cosmochim. Acta* **65**, 2677–2690 (2001).
- Panieri, G. et al. Diagenetic Mg-calcite overgrowths on foraminiferal tests in the vicinity of methane seeps. *Earth Planet. Sci. Lett.* **458**, 203–212 (2017).
- Loyd, S. J. & Smirnov, M. N. Progressive formation of authigenic carbonate with depth in siliciclastic marine sediments including substantial formation in sediments experiencing methanogenesis. *Chem. Geol.* **594**, 120775 (2022).
- Freitas, F. S. et al. Benthic organic matter transformation drives pH and carbonate chemistry in Arctic marine sediments. *Global Biogeochem. Cycles* **36**, e2021GB007187 (2022).
- Dessandier, P.-A. et al. Foraminiferal $\delta^{18}\text{O}$ reveals gas hydrate dissociation in Arctic and North Atlantic ocean sediments. *Geo-Mar. Lett.* **40**, 507–523 (2020).
- Kravchishina, M. D. et al. Authigenic Mg-calcite at a cold methane seep site in the Laptev Sea. *Oceanology* **57**, 174–191 (2017).
- Ruban, A., Rudmin, M., Dudarev, O. & Mazurov, A. The formation of authigenic carbonates at a methane seep site in the northern part of the Laptev Sea. *Minerals* **10**, 121103 (2020).
- Uchida, M. et al. Radiocarbon-based carbon source quantification of anomalous isotopic foraminifera in last glacial sediments in the western North Pacific. *Geochem. Geophys. Geosyst.* **9**, Q04N14 (2008).
- Wan, S., Feng, D., Chen, F., Zhuang, C. & Chen, D. Foraminifera from gas hydrate-bearing sediments of the northeastern South China Sea: proxy evaluation and application for methane release activity. *J. Asian Earth Sci.* **168**, 125–136 (2018).
- Panieri, G. et al. Record of methane emissions from the West Svalbard continental margin during the last 23,500 yrs revealed by $\delta^{13}\text{C}$ of benthic foraminifera. *Glob. Planet. Change* **122**, 151–160 (2014).
- Wycech, J., Kelly, D. C. & Marcott, S. Effects of seafloor diagenesis on planktic foraminiferal radiocarbon ages. *Geology* **44**, 551–554 (2016).
- Hong, W.-L., Lepland, A., Kirsimäe, K., Crémère, A. & Rae, J. W. B. Boron concentrations and isotopic compositions in methane-derived authigenic carbonates: constraints and limitations in reconstructing formation conditions. *Earth Planet. Sci. Lett.* **579**, 117337 (2022).
- Nørgaard-Pedersen, N. et al. Arctic Ocean during the Last Glacial Maximum: Atlantic and polar domains of surface water mass distribution and ice cover. *Paleoceanography* **18**, 1063 (2003).
- Knies, J., Vogt, C. & Stein, R. Late Quaternary growth and decay of the Svalbard/Barents Sea ice sheet and paleoceanographic evolution in the adjacent Arctic Ocean. *Geo-Mar. Lett.* **18**, 195–202 (1998).
- Synal, H. A., Stocker, M. & Suter, M. MICADAS: a new compact radiocarbon AMS system. *Nucl. Instrum. Meth. Phys. Res. B* **259**, 7–13 (2007).
- Ruff, M. et al. Gaseous radiocarbon measurements of small samples. *Nucl. Instrum. Methods Phys. Res.* **268**, 790–794 (2010).
- Nuernberg, D. Magnesium in tests of *Neogloboquadrina pachyderma* sinistral from high northern and southern latitudes. *J. Foramin. Res.* **25**, 350–368 (1995).
- Jonkers, L., Buse, B., Brummer, G.-J. A. & Hall, I. R. Chamber formation leads to Mg/Ca banding in the planktonic foraminifer *Neogloboquadrina pachyderma*. *Earth Planet. Sci. Lett.* **451**, 177–184 (2016).
- Bé, A. W. H. & Hemleben, C. Calcification in living planktonic foraminifer, *Globigerinoides sacculifer* (Brady). *N. Jahrb. Geol. Paläontol. Abh.* **134**, 221–234 (1970).
- Schiebel, R. & Hemleben, C. *Planktic Foraminifers in the Modern Ocean* (Springer, 2017).
- Vilks, G. Comparison of *Globorotalia pachyderma* (Ehrenberg) in the water column and sediments of the Canadian Arctic. *J. Foramin. Res.* **5**, 313–325 (1975).
- Schiebel, R. et al. Modern planktic foraminifers in the high-latitude ocean. *Mar. Micropaleontol.* **136**, 1–13 (2017).
- Aksu, A. E. & Vilks, G. Stable isotopes in planktonic and benthonic foraminifera from Arctic Ocean surface sediments. *Can. J. Earth Sci.* **25**, 701–709 (1987).
- Eynaud, F. et al. Morphological variability of the planktonic foraminifer *Neogloboquadrina pachyderma* from ACEX cores: implications for Late Pleistocene circulation in the Arctic Ocean. *Micropaleontology* **55**, 101–116 (2009).
- El Bani Altuna, N., Pieńkowski, A. J., Eynaud, F. & Thiessen, R. The morphotypes of *Neogloboquadrina pachyderma*: isotopic signature and distribution patterns in the Canadian Arctic Archipelago and adjacent regions. *Mar. Micropaleontol.* **142**, 13–24 (2018).
- Kohfeld, K. E., Fairbanks, R. G., Smith, S. L. & Walsh, I. D. *Neogloboquadrina pachyderma* (sinistral coiling) as paleoceanographic tracers in polar oceans: evidence from Northeast Water Polynya plankton tows, sediment traps and surface sediments. *Paleoceanography* **11**, 679–699 (1996).
- Livsey, C. M. et al. High-resolution Mg/Ca and $\delta^{18}\text{O}$ patterns in modern *Neogloboquadrina pachyderma* from the Fram Strait and Irminger Sea. *Paleoceanogr. and Paleoclimatol.* **35**, e2020PA003969 (2020).
- Srinivasan, M. S. & Kennett, J. P. Secondary calcification of the planktonic foraminifer *Neogloboquadrina pachyderma* as a climatic index. *Science* **186**, 630–632 (1974).
- Edgar, K. M., Anagnostou, E., Pearson, P. N. & Foster, G. L. Assessing the impact of diagenesis on $\delta^{11}\text{B}$, $\delta^{13}\text{C}$, $\delta^{18}\text{O}$, Sr/Ca and B/Ca values in fossil planktic foraminiferal calcite. *Geochim. Cosmochim. Acta* **166**, 189–209 (2015).
- Zamanian, K., Pustovoytov, K. & Kuzyakov, Y. Recrystallization of shell carbonate in soil: ^{14}C labeling, modeling and relevance for dating and paleo-reconstructions. *Geoderma* **282**, 87–95 (2016).
- Mekik, F. Radiocarbon dating of planktonic foraminifer shells: A cautionary tale. *Paleoceanography* **29**, 2013PA002532 (2013).
- Torres, M. E., Martin, R. A., Klinkhammer, G. P. & Nesbitt, E. A. Post depositional alteration of foraminiferal shells in cold seep settings: new insights from flow-through time-resolved analyses of biogenic and inorganic seep carbonates. *Earth Planet. Sci. Lett.* **299**, 10–22 (2010).
- Backman, J., Jakobsson, M., Lovlie, R., Polyak, L. & Febo, L. A. Is the central Arctic Ocean a sediment starved basin? *Quat. Sci. Rev.* **23**, 1435–1454 (2004).

48. Nürnberg, D. et al. Sediments in Arctic sea ice: implications for entrainment, transport and release. *Mar. Geol.* **119**, 185–214 (1994).
49. Geibert, W., Matthiessen, J., Stimac, I., Wollenburg, J. & Stein, R. Glacial episodes of a freshwater Arctic Ocean covered by a thick ice shelf. *Nature* **590**, 97–102 (2021).
50. Colombo, M. et al. Canadian arctic archipelago shelf-ocean interactions: a major iron source to Pacific derived waters transiting to the Atlantic. *Global Biogeochem. Cycles* **35**, e2021GB007058 (2021).
51. Stein, R. et al. Towards a better (litho-) stratigraphy and reconstruction of Quaternary paleoenvironment in the Amerasian Basin (Arctic Ocean). *Polarforschung* **79**, 97–121 (2010).
52. Fu, W. et al. Production of ancient dissolved organic carbon in arctic ocean sediment: a pathway of carbon cycling in the extreme environment. *Geophys. Res. Lett.* **47**, e2020GL087119 (2020).
53. Froitzheim, N., Majka, J. & Zastrozhnov, D. Methane release from carbonate rock formations in the Siberian permafrost area during and after the 2020 heat wave. *Proc. Natl Acad. Sci. USA* **118**, e2107632118 (2021).
54. Edmonds, H. N. et al. Discovery of abundant hydrothermal venting on the ultraslow-spreading Gakkel ridge in the Arctic Ocean. *Nature* **421**, 252–256 (2003).
55. Oakey, G. N. & Saltus, R. W. Geophysical analysis of the Alpha–Mendelevy ridge complex: characterization of the High Arctic Large Igneous Province. *Tectonophysics* **691**, 65–84 (2016).
56. Mackensen, A. & Nam, S.-I. Taxon-specific epibenthic foraminiferal $\delta^{18}\text{O}$ in the Arctic Ocean: relationship to water masses, deep circulation, and brine release. *Mar. Micropaleontol.* **113**, 34–43 (2014).
57. Meinhardt, A. K. et al. Diagenetic regimes in Arctic Ocean sediments: implications for sediment geochemistry and core correlation. *Geochim. Cosmochim. Acta* **188**, 125–146 (2016).
58. Honjo, S. et al. Biological pump processes in the cryopelagic and hemipelagic Arctic Ocean: Canada Basin and Chukchi Rise. *Prog. Oceanogr.* **85**, 137–170 (2010).
59. Zinkann, A.-C. et al. Depth distribution of organic carbon sources in Arctic Chukchi Sea sediments. *Deep Sea Res. II* **199**, 105076 (2022).
60. Rossel, P. E., Bienhold, C., Boetius, A. & Dittmar, T. Dissolved organic matter in pore water of Arctic Ocean sediments: environmental influence on molecular composition. *Org. Geochem.* **97**, 41–52 (2016).
61. Stein, R. & Macdonald, R. W. in *The Organic Carbon Cycle in the Arctic Ocean* (eds Stein, R. & Macdonald, R. W.) 315–322 (Springer Berlin Heidelberg, 2004).
62. Martens, J. et al. CASCADE – The Circum-Arctic Sediment Carbon DatabasE. *Earth Syst. Sci. Data* **13**, 2561–2572 (2021).
63. Bauch, D., Polyak, L. & Ortiz, J. D. A baseline for the vertical distribution of the stable carbon isotopes of dissolved inorganic carbon ($\delta^{13}\text{C}_{\text{DIC}}$) in the Arctic. *Ocean. Arktos* **1**, 15 (2015).
64. Uchida, M. et al. Age discrepancy between molecular biomarkers and calcareous foraminifera isolated from the same horizons of Northwest Pacific sediments. *Chem. Geol.* **218**, 73–89 (2005).
65. Tiwari, M., Nagoji, S., Kumar, V., Tripathi, S. & Behera, P. Oxygen isotope-salinity relation in an Arctic fjord (Kongsfjorden): Implications to hydrographic variability. *Earth Sci. Front.* **9**, 1937–1943 (2018).
66. Norgaard-Pedersen, N. *Late Quaternary Arctic Ocean Sediment Records: Surface Ocean Conditions and Provenance of Ice-Rafted Debris*. PhD thesis, GEOMAR Research Center for Marine Geosciences Christian Albrechts University in Kiel (1996).
67. Manizza, M. et al. Changes in the Arctic Ocean CO₂ sink (1996–2007): a regional model analysis. *Global Biogeochem. Cycles* **27**, 1108–1118 (2013).
68. Schrag, D. P., Higgins, J. A., Macdonald, F. A. & Johnston, D. T. Authigenic carbonate and the history of the global carbon cycle. *Science* **339**, 540 (2013).
69. Freitas, F. S. D. et al. Benthic organic matter transformation drives pH and carbonate chemistry in Arctic marine sediments. *Earth Space Sci. Open Arch.* **38**, e2021GB007187 (2022).
70. Stein, R. et al. *The Expedition ARKXXIII/3 of RV Polarstern in 2008*. Vol. 597 (ed Jokat, W.) 12–86 (Reports on Polar and Marine Research, 2009).
71. Molnár, Z., Pekker, P., Dódy, I. & Pósfai, M. Clay minerals affect calcium (magnesium) carbonate precipitation and aging. *Earth Planet. Sci. Lett.* **567**, 116971 (2021).
72. Scholze, C., Jørgensen, B. B. & Roy, H. Psychrophilic properties of sulfate-reducing bacteria in Arctic marine sediments. *Limnol. Oceanogr.* **66**, S293–S302 (2021).
73. Jørgensen, B. B., Laufer, K., Michaud, A. B. & Wehrmann, L. M. Biogeochemistry and microbiology of high Arctic marine sediment ecosystems—case study of Svalbard fjords. *Limnol. Oceanogr.* **66**, S273–S292 (2021).
74. Rogov, V. V., Kurchatova, A. N. & Taratunina, N. A. Types and micromorphology of authigenic carbonates in the Kolyma Yedoma Ice Complex, Northeast Siberia. *Front. Earth Sci.* **9**, 718904 (2021).
75. Jang, K. et al. Glacial freshwater discharge events recorded by authigenic neodymium isotopes in sediments from the Mendelev Ridge, western Arctic Ocean. *Earth Planet. Sci. Lett.* **369–370**, 148–157 (2013).
76. van Dijk, I., Raitzsch, M., Brummer, G.-J. A. & Bijma, J. Novel method to image and quantify cogwheel structures in foraminiferal shells. *Front. Ecol. Evol.* **8**, 567231 (2020).
77. Ausín, B. et al. Radiocarbon age offsets between two surface dwelling planktonic foraminifera species during abrupt climate events in the SW Iberian Margin. *Paleoceanogr. Paleoclimatol.* **34**, 63–78 (2019).
78. Polyak, L. Late Quaternary stratigraphy and sedimentation patterns in the western Arctic Ocean. *Glob. Planet. Change* **68**, 5–17 (2009).
79. Hillaire-Marcel, C., de Vernal, A., Rong, Y., Roberge, P. & Song, T. Challenging radiocarbon chronostratigraphies in central Arctic ocean sediment. *Geophys. Res. Lett.* **49**, e2022GL100446 (2022).
80. Heaton, T. J. et al. Marine20—The Marine Radiocarbon Age Calibration Curve (0–55,000 cal BP). *Radiocarbon* **62**, 779–820 (2020).
81. Geibert, W., Matthiessen, J., Wollenburg, J. & Stein, R. Reply to: No freshwater-filled glacial Arctic Ocean. *Nature* **602**, E4–E6 (2022).
82. Polyak, L. & Solheim, A. Late- and postglacial environments in the northern Barents Sea west of Franz Josef Land. *Polar Res.* **13**, 197–207 (1994).
83. Polyak, L., Curry, W. B., Darby, D. A., Bischof, J. & Cronin, T. M. Contrasting glacial/interglacial regimes in the western Arctic Ocean as exemplified by a sedimentary record from the Mendelev Ridge. *Palaeogeogr. Palaeoclimatol. Palaeoecol.* **203**, 73–93 (2004).
84. Bazhenova, E., Fagel, N. & Stein, R. North American origin of “pink–white” layers at the Mendelev Ridge (Arctic Ocean): new insights from lead and neodymium isotope composition of detrital sediment component. *Mar. Geol.* **386**, 44–55 (2017).
85. Vogt, C. Zeiliche und räumliche Verteilung von Mineralvergesellschaftungen in spätquartären Sedimenten des Arktischen Ozeans und ihre Nützlichkeit als Klimaindikatoren während der Glazial/Interglazial-Wechsel. *Repts. Polar Mar. Res.* **251**, 309 (1997).
86. Kravitz, J. H. *Sediments and Sediment Processes in Kane Basin, A High Arctic Glacial Marine Basin*. 184 (Institute of Arctic Alpine Res., University of Colorado, 1982).
87. Dalrymple, R. W. & Maass, O. Clay mineralogy of late Cenozoic sediments in the CESAR cores, Alpha Ridge, central Arctic Ocean. *Can. J. Earth Sci.* **24**, 1562–1569 (1987).
88. Fagel, N., Not, C., Gueibe, J., Mattioli, N. & Bazhenova, E. Late Quaternary evolution of sediment provenances in the Central Arctic Ocean: mineral assemblage, trace element composition and Nd and Pb isotope fingerprints of detrital fraction from the Northern Mendelev Ridge. *Quat. Sci. Rev.* **92**, 140–154 (2014).
89. Backman, J., Fornaciari, E. & Rio, D. Biochronology and paleoceanography of late Pleistocene and Holocene calcareous nannofossil abundances across the Arctic Basin. *Mar. Micropaleontol.* **72**, 86–98 (2009).
90. Levitan, M. A. Sedimentation rates in the Arctic Ocean during the last five marine isotope stages. *Oceanogr.* **55**, 425–433 (2015).
91. Spielhagen, R. F. et al. Arctic Ocean deep-sea record of northern Eurasian ice sheet history. *Quat. Sci. Rev.* **23**, 1455–1483 (2004).
92. Moore, D. M. & Reynolds, R. C. *X-ray Diffraction and the Identification and Analysis of Clay Minerals*. Vol. 38, 448 (Oxford University Press, 1997).
93. Tucker, M. E. *Techniques in Sedimentology* (Wiley, 1991).
94. Vogt, C., Lauterjung, J. & Fischer, R. Investigation of the clay fraction (<2 μm) of the clay mineral society reference clays. *Clays Clay Miner.* **50**, 388–400 (2002).
95. Petschick, R., Kuhn, G. & Gingele, F. Clay mineral distribution in surface sediments of the South Atlantic: sources, transport, and relation to oceanography. *Mar. Geol.* **130**, 203–229 (1996).
96. Mollenhauer, G., Grotheer, H., Torben, G., Bonk, E. & Hefter, J. Standard operation procedures and performance of the MICADAS radiocarbon laboratory at Alfred Wegener Institute (AWI), Germany. *Nucl. Instrum. Meth. Phys. Res. B* **496**, 45–51 (2021).
97. Coplen, T. B. New guidelines for reporting stable hydrogen, carbon, and oxygen isotope-ratio data. *Geochim. Cosmochim. Acta* **60**, 3359–3360 (1996).
98. Schlitzer, R. Ocean Data View. odv.awi.de (2023).
99. Hemleben, C., Spindler, M. & Anderson, O. R. *Modern Planktonic Foraminifera* (Springer, 1989).
100. Vogt, C. Bulk mineral assemblage of sediment core PS72/413-3 determined via full pattern QXRD. PANGAEA, <https://doi.org/10.1594/PANGAEA.945048> (2022).

Acknowledgements

We thank Victoria Afanasyeva, Thore Damman, Yara Zimmer, Christian Freuding and Chuling Zheng for their assistance in producing data and images on cores PS72/413-3 and PS2185-6. Ruth Cordelair assisted in the SEM work. Lisa Schönborn operated the

Thermo Fisher Scientific Finnigan MAT253 spectrometer. We thank the captain and crew of RV Polarstern for their excellent support during expeditions ARK-VIII/3 and ARK-XXVI/3. This study uses samples and data provided by the Alfred Wegener Institut Helmholtz-Zentrum für Polar- und Meeresforschung in Bremerhaven. Christian März, University of Bonn, Germany, shared with us his knowledge on porewater data and their influence on authigenic metal precipitates in the Arctic. We thank the XRD Lab Team (Johannes Birkenstock, Thomas Messner, Iris Spiess) for keeping the XRD diffractometer in perfect shape. We thank Sambuddha Misra and three unknown reviewers who helped to improve the manuscript.

Author contributions

J.E.W. designed the experiment, was in charge of the foraminifera work and the photographic documentation, and wrote the manuscript. J.M. assisted in writing. J.M. and C.V. contributed lithostratigraphic information and XRD results. J.E.W., W.G. and C.V. led the discussion on the origin of the authigenic overgrowth. J.E.W. and G.N. did the EDS analyses. D.W.-D. supervised the isotope measurements. H.G. and G.M. did the AMS dating. All co-authors contributed and commented on the manuscript.

Funding

Open Access funding enabled and organized by Projekt DEAL.

Competing interests

The authors declare no competing interests.

Additional information

Supplementary information The online version contains supplementary material available at <https://doi.org/10.1038/s43247-023-00802-9>.

Correspondence and requests for materials should be addressed to Jutta Erika Wollenburg.

Peer review information *Communications Earth & Environment* thanks Yanguang Liu, Sambuddha Misra and the other, anonymous, reviewer(s) for their contribution to the peer review of this work. Primary Handling Editors: Yama Dixit and Joe Aslin. Peer reviewer reports are available.

Reprints and permission information is available at <http://www.nature.com/reprints>

Publisher's note Springer Nature remains neutral with regard to jurisdictional claims in published maps and institutional affiliations.



Open Access This article is licensed under a Creative Commons Attribution 4.0 International License, which permits use, sharing, adaptation, distribution and reproduction in any medium or format, as long as you give appropriate credit to the original author(s) and the source, provide a link to the Creative Commons license, and indicate if changes were made. The images or other third party material in this article are included in the article's Creative Commons license, unless indicated otherwise in a credit line to the material. If material is not included in the article's Creative Commons license and your intended use is not permitted by statutory regulation or exceeds the permitted use, you will need to obtain permission directly from the copyright holder. To view a copy of this license, visit <http://creativecommons.org/licenses/by/4.0/>.

© The Author(s) 2023